

Research Article pubs.acs.org/acscatalysis

# Facet Impact of CuMn<sub>2</sub>O<sub>4</sub> Spinel Nanocatalysts on Enhancement of the Oxygen Reduction Reaction in Alkaline Media

Ming Zhou, Hongsen Wang, Lihua Zhang, Can Li, Amar Kumbhar, Héctor D. Abruña,\* and Jiye Fang\*



Cite This: ACS Catal. 2022, 12, 13663-13670



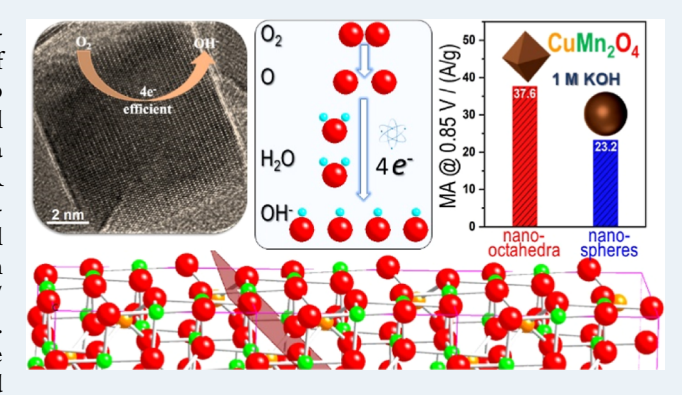
ACCESS I

Metrics & More

Article Recommendations

Supporting Information

ABSTRACT: Surface-structure engineering represents an attractive strategy to optimize the energy conversion performance of nanocatalysts using their deliberately controlled exposed facets. To further exploit the potential of non-Pt-group metal-based spinel catalysts for the alkaline oxygen reduction reaction (ORR), a cathodic fuel cell reaction, we hereby report a strategy of ORR improvement by controlling the crystallographic facets of ultrasmall CuMn<sub>2</sub>O<sub>4</sub> spinel nanocatalysts through a developed colloidal synthesis approach. The synthesis of CuMn<sub>2</sub>O<sub>4</sub> nanocrystals with morphological control relies on the design and selection of the Cu/ Mn precursors with striking discrepancies in reaction kinetics. Following carbon loading and an annealing post-treatment of the as-synthesized nanocatalysts, the exclusively {101} facet-exposed



CuMn<sub>2</sub>O<sub>4</sub> spinel nano-octahedra exhibit improved electrocatalytic activity toward the ORR in 1 M KOH, when compared to their spherical counterparts, exhibiting a mass activity (MA) of 37.6 A/g at 0.85 V. After 10,000 cycles of the ORR durability test, the nano-octahedra still retain an MA of 24.5 A/g, which is twice that of the CuMn<sub>2</sub>O<sub>4</sub> spinel nanospheres. Structural characterizations after durability testing indicate that the MA decay is likely associated with a decrease in the Mn<sup>3+</sup> fraction and the emergence of Cu<sup>+</sup> on CuMn<sub>2</sub>O<sub>4</sub> nano-octahedral surfaces. As a paradigm, this synthesis approach could be extended to other Mn-based spinel nanocatalysts with precise shape control, enabling us to understand and establish the relationship between the surface lattice/valence state and electrocatalytic properties.

KEYWORDS: nano-octahedron, spinel, ORR, alkaline media, CuMn2O4

### 1. INTRODUCTION

The oxygen reduction reaction (ORR) represents a significant electrocatalytic reaction in fuel cells, a class of transformative energy conversion technologies. Although many advances have been made in the widespread development of ORR catalysts for proton exchange membrane (PEM) fuel cells (i.e., acidic conditions), further mass utilization of this technology is impeded by the limit of the ORR catalysts including the need for precious metals such as platinum (Pt) or Pt-group metals (PGMs) and their sluggish kinetics. In alkaline fuel cells, alternatively, the PGM-containing expensive electrocatalysts can be replaced with a wide range of earth-abundant elementbased catalysts in a less corrosive environment, and the ORR is kinetically faster.

Transition metal spinel oxides are one class of state-of-theart catalysts that are potentially suitable for the ORR in alkaline media<sup>1-4</sup> and have been extensively studied due to their earth abundance, low cost, and access to multiple valence states. 5-8 To boost their electrocatalytic performance toward the ORR, 9-12 deliberately and precisely regulating the surface structure, at the atomic level, has been recognized as an effective strategy, which can fully combine and take advantage of the unique morphologies/facets and tunable chemical valence states. 8,13-15 Due to the lack of accessible synthetic approaches to tailor/control the exposed crystal facets, the underlying origination of how the surface structure affects catalytic performance has not been systematically investigated, resulting in an insufficient insight into crystal facet reactivity. Thus, the development of effective synthesis protocols for the preparation of spinel oxides in ultra-small sizes with welldefined facet control is still a formidable challenge. Moreover, further elucidating the relationships between the exclusive facets and their collective electrocatalytic behaviors is a rewarding endeavor due to the potentially significant impact on ORR performance improvement.

Similar to the fact that the crystallographic facet of PGMbased catalysts is an intimate factor associated with the ORR

Received: July 7, 2022 Revised: October 11, 2022 Published: October 25, 2022





performance in a PEM fuel cell,<sup>16-18</sup> it was experimentally determined that different facets on a spinel oxide and their diverse prorations of chemical valence states on the surfaces could also alter the catalytic performance. 13,19-21 Despite various efforts, 22-26 limited work on ORR performance of spinel oxides with controlled catalyst facets has been reported. Herein, we develop a facile and colloidal approach to prepare {101}-terminated CuMn<sub>2</sub>O<sub>4</sub> spinel nano-octahedra and demonstrate improved mass activity and durability toward the ORR in 1 M KOH solutions, when compared with those of their spherical counterparts. The experimental result indicates that control and tuning of the crystallographic facet, as a new strategic direction for the spinel electrocatalyst design, could also leverage the ORR performance in alkaline media. The motivation of this work is to explore the "shape effect" on ORR performance. As far as we know, such a kind of study on ultrasmall spinel electrocatalysts has never been reported.

#### 2. EXPERIMENTAL SECTION

**2.1. Chemicals.** Copper(II) chloride dihydrate (CuCl<sub>2</sub>·  $2H_2O$ ,  $\geq 99\%$ ), manganese(II) acetate tetrahydrate [Mn(Ac)<sub>2</sub>·  $4H_2O$ , 98%], copper(II) acetylacetonate [Cu(acac)<sub>2</sub>, 97%], oleylamine (OAm, 70%), oleic acid (OA, 90%), xylenes ( $\geq 98\%$ ), hexane ( $\geq 98.5\%$ ), ethanol (99.9%), chloroform (AR), potassium hydroxide (KOH,  $\geq 99.95\%$ ), 5% Nafion, and isopropanol (anhydrous, 99.5%) were purchased from Sigma-Aldrich and used as received without further purification. Ketjen Black EC600JD was provided by Lion Specialty Chemicals Co., Ltd. (JP). Deionized (DI) water with a resistivity of 18.2 MΩ·cm was obtained from a Purelab Flex3 water purification system (ELGA, UK).

2.2. Colloidal Synthesis of CuMn<sub>2</sub>O<sub>4</sub> Spinel Nano-Octahedra and Nanospheres. In a typical synthesis of CuMn<sub>2</sub>O<sub>4</sub> spinel nano-octahedra, CuCl<sub>2</sub>·2H<sub>2</sub>O (13.9 mg), Mn(Ac)<sub>2</sub>·4H<sub>2</sub>O (40.0 mg), OAm (2.6 mL), OA (1.3 mL), and xylene (6.0 mL) were combined in a 100 mL three-neck flask in an air atmosphere. The as-prepared mixture was sonicated for 6 min at room temperature to help dissolve all the solids completely and then heated to 90 °C at 5 °C/min under vigorous magnetic stirring. After 20 min, DI water (1.0 mL) was rapidly introduced into the aforementioned mixture using a syringe. Subsequently, the resultant solution was aged at 90 °C for 24 h and then cooled to room temperature naturally. Finally, the products were precipitated using a mixture of hexane and ethanol (5.0 mL/15.0 mL) and collected by centrifugation at 9,000 rpm for 10 min. After further washing twice using a mixture of hexane and ethanol (v/v = 1:2) followed by centrifugation, the nanocrystals were re-dispersed in 5.0 mL of hexane as stock suspensions.

For the synthesis of CuMn<sub>2</sub>O<sub>4</sub> spinel nanospheres, a similar protocol was applied, except for the substitution of CuCl<sub>2</sub>· 2H<sub>2</sub>O with Cu(acac)<sub>2</sub> (21.4 mg).

**2.3. Characterizations.** X-ray diffraction (XRD) patterns were recorded from 25 to  $80^{\circ}$  ( $2\theta$ ) using a scan rate of  $2^{\circ}$  min<sup>-1</sup> at a step size of  $0.02^{\circ}$  on a Rigaku Ultima IV diffractometer. X-ray photoelectron spectroscopy (XPS) spectra were acquired on PHI 5000 VersaProbe equipment. Transmission electron microscopy (TEM) and high-resolution TEM (HRTEM) images were taken using JEOL JEM-2100F (Japan) operated at 200 kV. The TEM/HRTEM samples were prepared by drop-casting the nanocrystal dispersions in hexane on amorphous carbon-coated Cu grids and drying under ambient conditions. Energy-dispersive X-ray spectroscopy

(EDX) analysis together with partial scanning TEM (STEM) images was carried out in the STEM mode on amorphous carbon-coated Au grids using an aberration-corrected JEOL 2200FS electron microscope equipped with a Bruker-AXS silicon drift detector and an FEI Talos 200X. The metal compositions in samples were analyzed using inductively coupled plasma-optical emission spectroscopy (ICP-OES, Optima 7000 DV).

2.4. Working Electrode Preparation. The CuMn<sub>2</sub>O<sub>4</sub> spinel nano-octahedra and nanospheres were loaded on active carbon (Ketjen Black EC600JD). Briefly, the CuMn<sub>2</sub>O<sub>4</sub> spinel nanocrystals (4.0 mg) and Ketjen Black (6.0 mg) were mixed with ethanol (5.0 mL) under ultrasonication for 4 h. The carbon-supported CuMn<sub>2</sub>O<sub>4</sub> spinel nanocrystals were then collected by centrifugation (9,000 rpm for 10 min). Subsequently, they were redispersed in an ethanol solution containing 0.1 M KOH and isolated by centrifugation thrice. The KOH-treated sample was further annealed in air at 300 °C for 12 h to help remove the surfactants absorbed on the surface of the nanocrystals. Next, the carbon-supported catalysts (5.0 mg, CuMn<sub>2</sub>O<sub>4</sub> nano-octahedra/C or nanospheres/C) were redispersed in a mixture of DI water (0.6 mL), isopropanol (0.4 mL), and 5% Nafion (10.0  $\mu$ L) under ultrasonication for 1 h. The resultant ink (10.0  $\mu$ L) was drop-casted on a precleaned glassy carbon (GC) rotating disk electrode (RDE) (diameter: 5 mm) provided by Pine Research Instrumentation and dried at room temperature under ambient conditions. Similarly, the Pt/C catalyst containing 20 wt % Pt supported on Vulcan XC-72R (from Fuel Cell Store) was used as a reference for comparison. The Pt/C catalyst ink was produced by dispersing the Pt/C catalysts (2.0 mg) in a mixture containing isopropanol (1.0 mL), DI water (1.0 mL), and 5% Nafion (20.0  $\mu$ L) under ultrasonication for ~2 h. Then, the Pt/C catalyst ink (20.0  $\mu$ L) was loaded on a pre-cleaned GC RDE and dried in the same way. The Pt mass loading of the commercial Pt/C catalysts is thus 20.0  $\mu$ g/cm<sup>2</sup>.

**2.5. Electrochemical Measurements.** All electrochemical evaluations were conducted on an electrochemical workstation (Gamry, 1000E) using a three-neck electrochemical cell at room temperature. The cell was pre-washed using aqua regia and then rinsed thoroughly using DI water to avoid any potential contamination. A GC RDE (geometric area:  $0.196~\rm cm^2$ ) loaded with catalysts was utilized as the working electrode. Ag/AgCl in saturated KCl solution and a graphite rod were employed as the reference and counter electrodes, respectively. All potentials were converted to those vs the reversible hydrogen electrode (RHE), or  $V_{\rm RHE}$ , using the following equation

$$E(RHE) = E(Ag/AgCl) + 1.0258(V)$$

The working electrodes were initially cycled between 0.10 and 1.42 V at a rate of 50 mV s $^{-1}$  in Ar-saturated 1 M KOH for 50 cycles to remove the remaining species from the catalyst surfaces and yield stable cyclic voltammetry (CV) profiles. The working electrodes were then scanned cathodically between 0.38 and 1.09 V at 5 mV s $^{-1}$  and 1,600 rpm in O<sub>2</sub>-saturated 1 M KOH. Note that the capacitive background currents in CV curves measured in Ar-saturated 1 M KOH solution were subtracted from the raw ORR data. All the current densities shown in CV and ORR profiles were worked out based on the electrode geometric area only. An accelerated durability test (ADT) was performed by potential cyclings from 0.6 to 1.0 V at 100 mV s $^{-1}$  in the O<sub>2</sub>-saturated 1 M KOH electrolyte for a

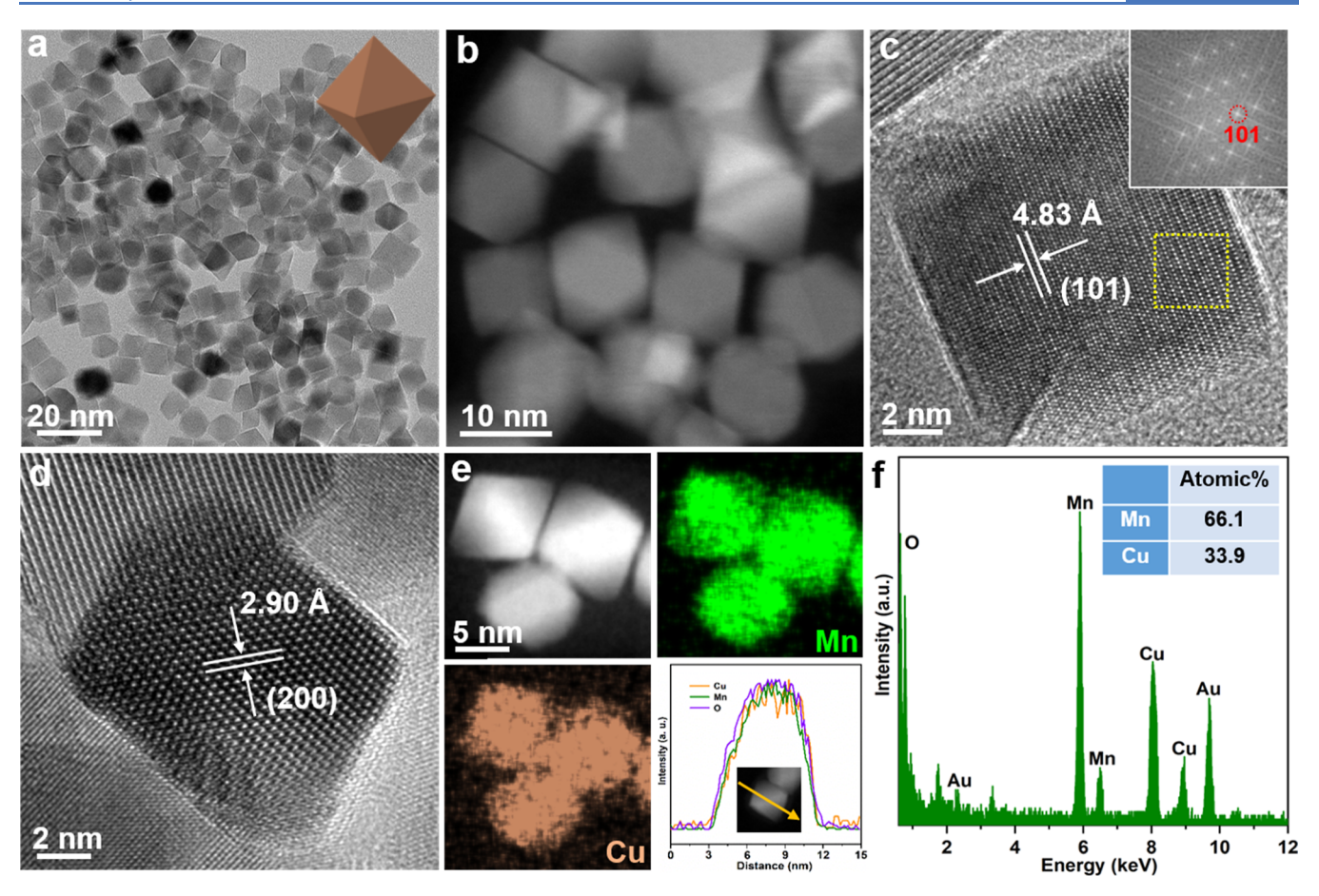


Figure 1. (a) Low-magnification TEM and (b) HAADF-STEM images of the as-prepared  $CuMn_2O_4$  nano-octahedra. (c,d) HRTEM images of a representative  $CuMn_2O_4$  nano-octahedron. (e) STEM image, elemental mappings, and the corresponding normalized EDX line scan of a representative  $CuMn_2O_4$  nano-octahedron. (f) STEM-EDX spectrum of the  $CuMn_2O_4$  nano-octahedra. The inset in (a) displays the 3D model of the octahedral nanocrystals corresponding to the TEM image. The inset in (c) shows the corresponding FFT pattern taken from the yellow dashed square in (c). The inset in (f) shows the atomic percentage of the Mn and Cu elements in the  $CuMn_2O_4$  nano-octahedra.

maximum of 10,000 cycles. To avoid potential contamination from metal species in the solution, the ORR profiles after 10,000 cycles were obtained in a fresh  $\rm O_2$ -saturated 1 M KOH solution.

### 3. RESULTS AND DISCUSSION

In the CuMn<sub>2</sub>O<sub>4</sub> nanocrystal preparation, we believe that OAm provides an alkalescent environment for the synthesis, and OA regulates the alkalinity of the reaction solution, whereas xylene serves as a non-polar solvent. Following the injection of water, the color of the reaction mixture immediately turned brick red, indicating a prompt generation of bimetallic Cu-Mn hydroxides as reaction intermediates. Based on the well-known conversion mechanisms between the hydroxides and oxides of  $Cu^{27-29}$  and Mn,  $^{30}$  it is believed that these intermediate species could be further facilitated into the CuMn<sub>2</sub>O<sub>4</sub> spinel in the following aging process. Figure 1a,b presents low-magnification TEM and high-angle annular darkfield STEM (HAADF-STEM) images of the as-synthesized CuMn<sub>2</sub>O<sub>4</sub> nano-octahedra, showing a narrow size distribution with an average edge length of  $9.1 \pm 0.9$  nm (Figure S1) and a yield for octahedra of higher than 90%. The HRTEM images (Figure 1c,d) taken from a representative octahedron displayed high crystallinity with a continuous lattice extending across the entire facet. The tetragonal structure can be further identified from the corresponding fast Fourier transform (FFT) pattern

taken from the yellow dashed square in Figure 1c. The lattice spacings were determined as 4.83 and 2.90 Å, matching the (101) and (200) planes, respectively. These observations further confirm that the as-synthesized octahedral nanocrystals are single-crystal structures terminated with pure {101} facets. The spatial dispersion of Mn and Cu in an octahedron was resolved by EDX elemental mapping and line scans, from which the uniform dispersion of Mn and Cu across the entire nanocrystal could be observed (Figure 1e). The Mn/Cu atomic ratio of a CuMn<sub>2</sub>O<sub>4</sub> nano-octahedron was also analyzed by STEM-EDX (Figure 1f), yielding a value of 1.95, which is well consistent with ICP-OES results (Mn/Cu atomic ratio = 1.97:1). These analyses suggest that the fraction of the element Cu in the one-pot synthesized CuMn<sub>2</sub>O<sub>4</sub> nano-octahedra is slightly higher than its spinel stoichiometric composition (vide infra).

As a comparative study,  $\text{CuMn}_2\text{O}_4$  nanospheres were also synthesized using the same protocol using  $\text{Cu}(\text{acac})_2$  instead of  $\text{CuCl}_2 \cdot 2\text{H}_2\text{O}$  as an alternative Cu precursor. As shown in Figure S2a,b, the as-synthesized  $\text{CuMn}_2\text{O}_4$  nanospheres displayed a narrow size distribution with an average size of  $7.8 \pm 1.1$  nm. The explicit lattice fringes with a spacing of 4.85 Å, as revealed in Figure S2c, can be assigned to the (101) plane of tetragonal  $\text{CuMn}_2\text{O}_4$ . In contrast to those of the octahedral case, the Mn/Cu atomic ratios in the nanospheres determined from both STEM-EDX (Figure S2d) and ICP-OES were 2.02

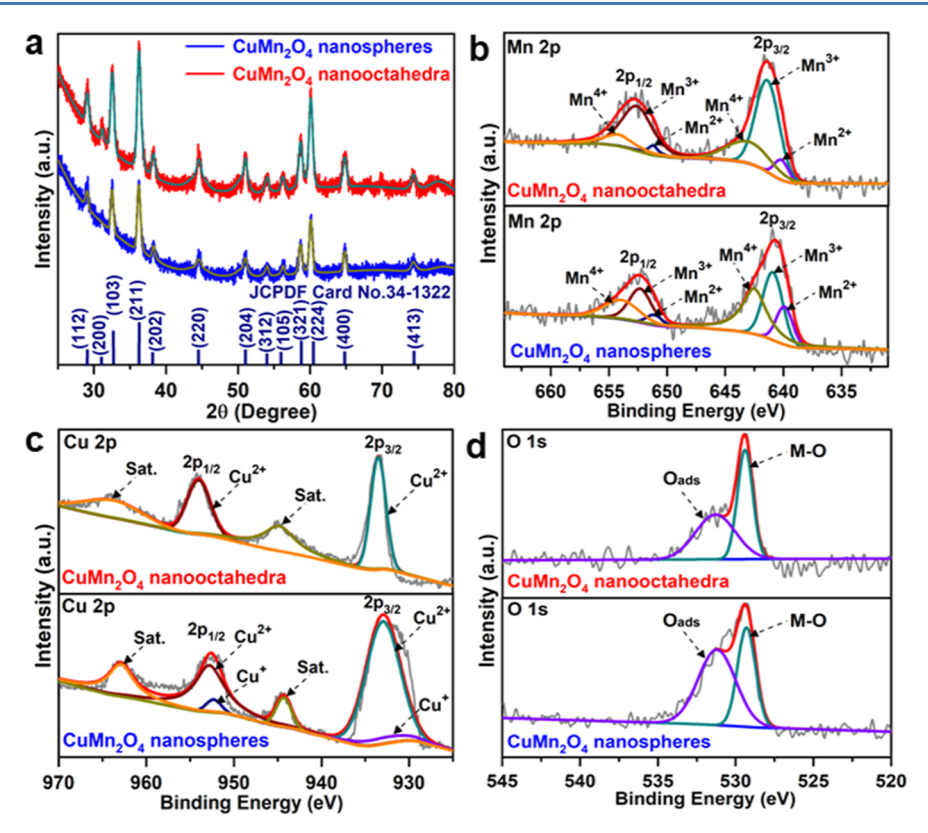


Figure 2. (a) XRD patterns of carbon-supported  $CuMn_2O_4$  nano-octahedra and nanospheres after heating in air at 300 °C for 12 h. (b–d) XPS spectra of Mn 2p (b), Cu 2p (c), and O 1s (d) for carbon-supported  $CuMn_2O_4$  nano-octahedra and nanospheres after heating in air at 300 °C for 12 h. Relative ratios of element states: for nano-octahedra,  $Mn^{2+}/Mn^{3+}/Mn^{4+} = 8.76:16$  and  $Cu^{2+}/Cu^{+} = 100:0$ .; For nanospheres,  $Mn^{2+}/Mn^{3+}/Mn^{4+} = 14:58:28$  and  $Cu^{2+}/Cu^{+} = 93:7$ .

and 2.07, respectively, showing a slightly lower Cu fraction when compared with its spinel stoichiometric proportion. We attribute the different Cu contents in both types of products to the diverse conversion rates of the Cu precursors. It is well known that the bi-dentate acetylacetonate ligand from the input precursor [in this work, Cu(acac)<sub>2</sub>] binds the cations more strongly than the mono-dentate ligands do<sup>31</sup> (in this work, chloride). The formation of octahedral CuMn<sub>2</sub>O<sub>4</sub> nanocrystals is benefited from the relatively fast release of cupric ions followed by a synergistic growth with the manganese lattices, whereas the sluggish delivery of cupric ions due to the stronger binding effect from the acetylacetonate ligand delayed the supply of sufficient cupric ions to the development of shape-controlled nanocrystals. Consequently, we elucidate that the morphologies (octahedron vs sphere) of CuMn<sub>2</sub>O<sub>4</sub> nanocrystals mainly originate from the reactivity of the Cu precursors, and this can be partially supported by the different Cu fractions in both products when the molar proportion and equivalent quantity of the input precursors are the same in both cases.

Both the  $\text{CuMn}_2\text{O}_4$  samples were subsequently loaded onto carbon and annealed in air at 300 °C for 12 h to receive  $\text{CuMn}_2\text{O}_4$  nano-octahedra/C and  $\text{CuMn}_2\text{O}_4$  nanospheres/C catalysts. These carbon-supported samples were analyzed using XRD to confirm their crystal structures. The annealing treatment in air could further improve the crystallinity of these catalysts and effectively remove the surfactants adsorbed on their surfaces, thereby facilitating the ORR catalytic reaction. As presented in Figure 2a, all the characteristic peaks in the XRD patterns of both samples displayed well-resolved diffraction peaks, matching the standard lines of

tetragonal CuMn<sub>2</sub>O<sub>4</sub> well (JCPDS no. 34-1322). This confirms the existence of the tetragonal phase with high crystallinity. To identify the valence states of Mn, Cu, and O and the surface composition of these nanocrystals supported on carbon, XPS measurements were carried out. As revealed in Figure S3, the XPS survey spectrum of the CuMn<sub>2</sub>O<sub>4</sub> nano-octahedra/C suggests the copresence of Mn, Cu, and O, in which the molar ratio between Mn and Cu was determined as 1.98:1. This is almost the same as the STEM-EDX and ICP-OES results, indicating the uniform composition dispersion throughout the entire nanocrystal. The Mn 2p spectra of CuMn<sub>2</sub>O<sub>4</sub> nanooctahedra/C and nanospheres/C (Figure 2b) were best fitted to three spin-orbit doublet characteristics of Mn<sup>2+</sup> (640.4 and 651.6 eV), Mn3+ (641.6 and 652.8 eV), and Mn4+ (643.2 and 654.4 eV), in which the surfaces of these CuMn<sub>2</sub>O<sub>4</sub> nanocrystals were mainly dominated by Mn<sup>3+</sup> (Mn<sup>4+</sup>/Mn<sup>3+</sup>/  $Mn^{2+} = 16/76/8$ ). Notably, all the peaks of  $CuMn_2O_4$  nanooctahedra/C exhibited slightly positive shifts compared to the peak positions of CuMn<sub>2</sub>O<sub>4</sub> nanospheres/C, indicating an appreciable change in the electronic structure of Mn in CuMn<sub>2</sub>O<sub>4</sub> nano-octahedra/C. More importantly, the Mn<sup>3+</sup> content in CuMn<sub>2</sub>O<sub>4</sub> nano-octahedra/C was determined to be 76%, which is much higher than that in CuMn<sub>2</sub>O<sub>4</sub> nanospheres/C ( $Mn^{3+} = 58\%$ ). The high content of  $Mn^{3-}$ might be more beneficial to boosting the ORR performance. This result is consistent with the previous reports in which the ORR activity is strongly associated with the surface Mn valence states of Mn-based spinel oxides.<sup>6,35</sup> For the Cu 2p spectra illustrated in Figure 2c, the peaks positioned at 933.5 and 954.0 eV in CuMn<sub>2</sub>O<sub>4</sub> nano-octahedra/C can be assigned to Cu<sup>2+</sup>, which are more positive than those in CuMn<sub>2</sub>O<sub>4</sub>

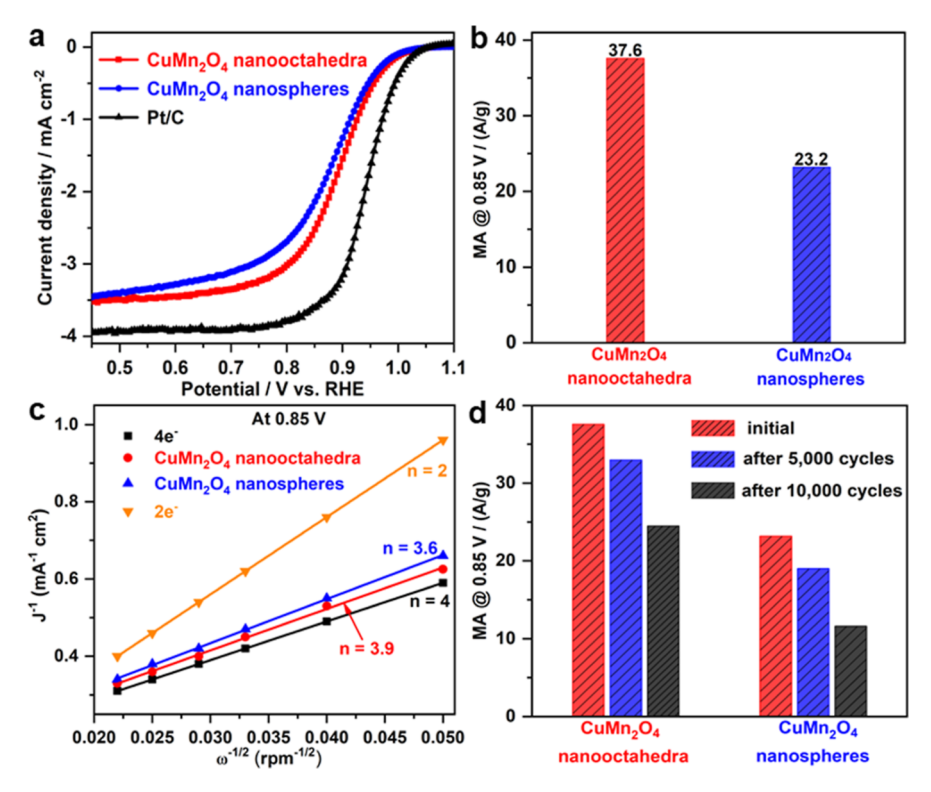


Figure 3. (a) ORR polarization profiles of CuMn<sub>2</sub>O<sub>4</sub> nano-octahedra/C, CuMn<sub>2</sub>O<sub>4</sub> nanospheres/C, and commercial Pt/C, in O<sub>2</sub>-saturated 1 M KOH at a scan rate of 5 mV/s at 1,600 rpm. Mass loading of CuMn<sub>2</sub>O<sub>4</sub> and Pt: 100 and 20 μg/cm². (b) Mass activities of CuMn<sub>2</sub>O<sub>4</sub> nano-octahedra/C and CuMn<sub>2</sub>O<sub>4</sub> nanospheres/C at 0.85 V vs RHE, which were calculated by normalizing the kinetic current to the mass loading of the metal oxide on the electrode. (c) K–L plots (J<sup>-1</sup>vs ω<sup>-1/2</sup>) of CuMn<sub>2</sub>O<sub>4</sub> nano-octahedra/C and CuMn<sub>2</sub>O<sub>4</sub> nanospheres/C derived from the RDE voltammograms at 0.85 V. (d) Mass activities of CuMn<sub>2</sub>O<sub>4</sub> nano-octahedra/C and CuMn<sub>2</sub>O<sub>4</sub> nanospheres/C before and after the ADTs in O<sub>2</sub>-saturated 1 M KOH at 0.85 V vs RHE. Note that all the current densities in (a) and (c) are based on the electrode geometric area.

nanospheres/C, confirming a clear change of the electronic structure of Cu in CuMn<sub>2</sub>O<sub>4</sub> nano-octahedra/C as well. It was previously reported that the presence of Cu<sup>+</sup> affects the longrange cation ordering in spinels and thus lowers the crystal symmetry.<sup>36–38</sup> In Figure 2c, no Cu<sup>+</sup> peaks were observed in CuMn<sub>2</sub>O<sub>4</sub> nano-octahedra/C, further implying the much stronger structural stability in nano-octahedra relative to nanospheres. Moreover, the deconvoluted O 1s spectra in Figure 2d, which were fitted by two components assigned as lattice oxygen located at 529.3 eV and oxygen-containing species adsorbed on the surface, located at 531.3 eV, suggest a larger number of lattice oxygens on CuMn2O4 nanooctahedra/C than those on CuMn<sub>2</sub>O<sub>4</sub> nanospheres/C. It should be pointed out that the large presence of lattice oxygen significantly contributes to the O2 binding, thus greatly improving the ORR performance in alkaline media. 39,40 Taking together, these results reveal that the CuMn2O4 nanooctahedra/C exhibited enhanced electronic interactions (between Cu and Mn centers), high chemical/structural stability, and improved ability of O2 adsorption when compared with the CuMn<sub>2</sub>O<sub>4</sub> nanospheres/C. These features should potentially improve the performance of nanooctahedra/C toward the ORR in alkaline media.

The electrocatalytic performance of the CuMn $_2O_4$  nano-octahedra/C, nanospheres/C, and commercial Pt/C for the ORR was comparatively investigated in 1 M KOH solution using an RDE. Figure 3a shows the positive-going ORR polarization curves determined from the CuMn $_2O_4$  nano-octahedra/C, CuMn $_2O_4$  nanospheres/C, and commercial Pt/C catalysts. In Figure 3a, the CuMn $_2O_4$  nano-octahedra/C

show an  $E_{1/2}$  value of 0.881 V *versus* RHE, which is 17 mV higher than that of the CuMn<sub>2</sub>O<sub>4</sub> nanospheres/C, indicating higher ORR catalytic activity of the CuMn<sub>2</sub>O<sub>4</sub> nano-octahedra/C catalyst compared with that of the CuMn<sub>2</sub>O<sub>4</sub> nanospheres/C. More importantly, the ORR polarization profiles of both CuMn<sub>2</sub>O<sub>4</sub> samples revealed a diffusion-limited current density of -3.6 mA/cm<sup>2</sup>, similar to that of the case of commercial Pt/C, indicating a dominant  $4e^-$  reduction process accompanied by the complete conversion of O<sub>2</sub> into H<sub>2</sub>O.

Unlike Pt or other transition metal electrocatalysts, for which the electrochemically active surface area (ECSA) can be typically determined using hydrogen underpotential deposition (H<sub>UPD</sub>) or CO-stripping methods, it is quite challenging to accurately evaluate the ECSA of oxide electrocatalysts, although several methods have been under development. 41-43 For comparison, we adopt a general approach to roughly estimate the ECSAs of the CuMn<sub>2</sub>O<sub>4</sub> nano-octahedra and nanospheres on the basis of the CV curves in the capacitive region in N2-saturated 1 M KOH. The ECSA value of the  $CuMn_2O_4$  nano-octahedra/C was calculated as 72.6 m<sup>2</sup>/g, which is about 1.5-fold as high as that of the CuMn<sub>2</sub>O<sub>4</sub> nanospheres/C ( $48.4 \text{ m}^2/\text{g}$ ). Note that a reference capacitance value of 40  $\mu$ F/cm<sup>2</sup> was assumed. As exemplified in the recent literature, 2,44-47 in this work, we only focus on the mass activity-based assessment due to the lack of a benchmark ECSA measurement approach for spinels. To further assessably evaluate the activity, the MA at 0.85 V (used as a metric value) was calculated based on the Levich equation and further normalized against the mass loading of metal oxides on the electrode. As summarized in Figure 3b, the MA at 0.85 V of the CuMn<sub>2</sub>O<sub>4</sub> nano-octahedra/C (37.6 A/g) was about 1.62 times as high as that of the  $CuMn_2O_4$  nanospheres/C (23.2 A/ g). Assuming that the carbon-supported annealing at 300 °C would not change the particle size much, the possible size effect on this ORR performance of both the CuMn<sub>2</sub>O<sub>4</sub> nanocatalysts can be ruled out based on the estimation of their specific surface areas (refer to the discussion in the Supporting Information). Relative to the CuMn<sub>2</sub>O<sub>4</sub> nanosphere/C catalyst, the enhanced MA of the CuMn<sub>2</sub>O<sub>4</sub> nanooctahedral/C catalyst can thus be mainly attributed to the exclusively exposed {101} facets on the catalyst surface and a higher Mn<sup>3+</sup> content. The corresponding Koutecky-Levich (K-L) plots (J<sup>-1</sup> $\nu s \omega^{-1/2}$ ) derived from the RDE voltammograms (Figure S4a,b) at 0.85 V are presented in Figure 3c. The K-L plots show good linearity and parallelism for the CuMn<sub>2</sub>O<sub>4</sub> nano-octahedral/C and CuMn<sub>2</sub>O<sub>4</sub> nanosphere/C catalysts, revealing the first-order reaction kinetics for the ORR as a function of the concentration of dissolved oxygen. In addition, the electron transfer numbers (n) at +0.85 V were determined to be ~3.9 for the CuMn<sub>2</sub>O<sub>4</sub> nano-octahedral/C catalyst and ~3.6 for the CuMn<sub>2</sub>O<sub>4</sub> nanosphere/C catalyst, further verifying their excellent ORR activity.

The durability of the CuMn<sub>2</sub>O<sub>4</sub> nano-octahedral/C catalyst was evaluated via an ADT, demonstrating a remarkable enhancement in stability when compared to that of the CuMn<sub>2</sub>O<sub>4</sub> nanosphere/C and Pt/C catalysts. As exhibited in Figure S5a, the CuMn<sub>2</sub>O<sub>4</sub> nano-octahedral/C catalyst showed an activity decay with a  $\Delta E_{1/2}$  value of 10 mV after 5,000 cycles and 24 mV after 10,000 cycles, which is superior to that of the  $\text{CuMn}_2\text{O}_4$  nanospheres/C with a  $\Delta E_{1/2}$  value of 33 mV (Figure S5b) and the commercial Pt/C with a  $\Delta E_{1/2}$  value of 51 mV after 10,000 cycles (Figure S5c). The MA of the CuMn<sub>2</sub>O<sub>4</sub> nano-octahedral/C catalyst at 0.85 V decreased from 37.6 to 33.0 A/g after 5,000 cycles, equivalent to a loss of 12% relative to the pristine MA (Figure 3d). After 10,000 cycles, the CuMn<sub>2</sub>O<sub>4</sub> nano-octahedral/C catalyst retained 65.2% of its original MA value, while the CuMn<sub>2</sub>O<sub>4</sub> nanosphere/C catalyst only retained 50% of its initial value (Figure 3d). Remarkably, the MA of the CuMn<sub>2</sub>O<sub>4</sub> nanooctahedral/C catalyst after 10,000 cycles was about 2 times as high as that of the CuMn<sub>2</sub>O<sub>4</sub> nanosphere/C catalyst. Based on the CV measurements before and after the ADT (Figure S6ac), the CuMn<sub>2</sub>O<sub>4</sub> nano-octahedral/C, CuMn<sub>2</sub>O<sub>4</sub> nanosphere/ C, and Pt/C catalysts displayed a continuous decrease in the ECSA, mainly due to the nanoparticle aggregation/sintering and the loss of active components during the ADT progress. To probe the origin of the catalytic activity decline after the ADT, TEM (Figure S7a), HAADF-STEM (Figure S7b), and HRTEM characterizations (Figure S7c) were further performed to examine the size, morphology, and crystal phase changes for the CuMn<sub>2</sub>O<sub>4</sub> nano-octahedral/C catalyst. Impressively, after the ADT, the CuMn<sub>2</sub>O<sub>4</sub> nano-octahedral/ C catalyst retained its pristine structural parameters. The uniform elemental distribution in a representative carbonsupported CuMn<sub>2</sub>O<sub>4</sub> nano-octahedron, after the ADT, was further confirmed by EDX mapping and a corresponding normalized EDX line scan (Figure S7d), in which the ratio of Mn/Cu was determined to be 2.2:1. Meanwhile, the XPS characterization (Figure S8) was carried out to determine the valence states of Mn and Cu on the catalyst surface after the 10,000-cycle ADT, in which the ratio of Mn/Cu was determined to be 2.3:1, nearly consistent with the EDX results. Especially, the content of Mn<sup>3+</sup> (Figure S8a) shows a

significant diminution from 76% (before the ADT) to 58% (after the 10,000-cycle ADT), illustrating the intrinsic nature of the ORR activity decline. Further XPS analysis of the Cu 2p spectrum (Figure S8b) revealed the appearance of Cu<sup>+</sup> peaks, although Cu<sup>2+</sup> was still the dominant state of Cu atoms in the CuMn<sub>2</sub>O<sub>4</sub> nano-octahedral/C catalyst after the ADT. The presence of Cu<sup>+</sup> may also contribute to an effect on the cation ordering, leading to degradation in the structural stability and ORR activity of the catalyst, as reported in previous studies. 36,38 As a result, we posit that the ORR activity decline in the CuMn<sub>2</sub>O<sub>4</sub> nano-octahedral/C catalyst after the ADT could arise, at least in part, from a decrease in the surface Mn<sup>3+</sup> content and the appearance of Cu<sup>+</sup>. Taken together, the aforementioned results demonstrate that the CuMn<sub>2</sub>O<sub>4</sub> nanooctahedral/C catalyst shows enhanced ORR performance than its spherical counterpart with both enhanced mass activity and durable stability. The determined mass activity is also superior to the values from most of the recently reported spinel electrocatalysts (Table S1).

#### 4. CONCLUSIONS

We demonstrate a facile, colloidal approach for a rational synthesis of uniform CuMn<sub>2</sub>O<sub>4</sub> spinel nanocrystals with a welldefined morphology and size and specific Mn3+/Mn2+ and Cu<sup>2+</sup>/Cu<sup>+</sup> ratios on the surface. We uncovered that the type of Cu precursor plays a pivotal role in facilitating/controlling the formation of CuMn2O4 nanocrystals with distinct morphologies. More importantly, the as-synthesized CuMn<sub>2</sub>O<sub>4</sub> spinel nano-octahedra exhibited improved electrocatalytic activity and stability toward the ORR in alkaline media when compared with their nano-spherical counterparts. It was found that the ORR activity decay may be due to a decrease in the Mn<sup>3+</sup> content and the existence of Cu<sup>+</sup> on the surface of the CuMn<sub>2</sub>O<sub>4</sub> nano-octahedral catalyst. This work provides a new strategy in crystal facet-controlled synthesis of CuMn<sub>2</sub>O<sub>4</sub> nanocrystals with substantially enhanced ORR performance. The facet-tailored nanocatalysts with distinctive surface valence states could provide a unique platform for an in-depth understanding of their surface lattice- and valence-statedependent catalytic properties.

#### ASSOCIATED CONTENT

### Supporting Information

The Supporting Information is available free of charge at https://pubs.acs.org/doi/10.1021/acscatal.2c03275.

Supporting figures and table and discussion (PDF)

### AUTHOR INFORMATION

### **Corresponding Authors**

Héctor D. Abruña — Department of Chemistry and Chemical Biology, Cornell University, Ithaca, New York 14853, United States; orcid.org/0000-0002-3948-356X; Email: hda1@cornell.edu

Jiye Fang — Department of Chemistry, State University of New York at Binghamton, Binghamton, New York 13902, United States; Occid.org/0000-0003-3703-3204; Email: jfang@binghamton.edu

### Authors

Ming Zhou — Department of Chemistry, State University of New York at Binghamton, Binghamton, New York 13902, United States; Occid.org/0000-0002-2708-0501

- Hongsen Wang Department of Chemistry and Chemical Biology, Cornell University, Ithaca, New York 14853, United States; © orcid.org/0000-0001-7926-2895
- Lihua Zhang Center for Functional Nanomaterials, Brookhaven National Laboratory, Upton, New York 11973, United States
- Can Li Department of Chemistry, State University of New York at Binghamton, Binghamton, New York 13902, United States; orcid.org/0000-0001-8894-5110

Amar Kumbhar — Chapel Hill Analytical and Nanofabrication Laboratory, The University of North Carolina at Chapel Hill, Chapel Hill, North Carolina 27599, United States

Complete contact information is available at: https://pubs.acs.org/10.1021/acscatal.2c03275

#### **Notes**

The authors declare no competing financial interest.

#### ACKNOWLEDGMENTS

This work was primarily supported by the Center for Alkaline-Based Energy Solutions (CABES), an Energy Frontier Research Center funded by the U.S. Department of Energy, Office of Science, Basic Energy Sciences, under award # DE-SC0019445. M.Z. and C.L. were also partially supported by the National Science Foundation under grant # DMR 1808383. L.Z. acknowledges the use of TEM facilities for the structural characterizations, at the Center for Functional Nanomaterials, Brookhaven National Laboratory, which is supported by the U.S. DOE, Office of Science, Basic Energy Sciences, under contract no. DE-SC0012704. M.Z. thanks Yingqing Ou and Anju Sharma for their help in XPS measurement at the University of Oregon and the State University of New York at Binghamton, respectively. Partial low-magnification TEM imaging work was supported by S3IP/ADL, State University of New York at Binghamton.

### REFERENCES

- (1) Ge, X.; Sumboja, A.; Wuu, D.; An, T.; Li, B.; Goh, F. W. T.; Hor, T. S. A.; Zong, Y.; Liu, Z. Oxygen Reduction in Alkaline Media: From Mechanisms to Recent Advances of Catalysts. *ACS Catal.* **2015**, *5*, 4643–4667.
- (2) Yang, Y.; Xiong, Y.; Holtz, M. E.; Feng, X.; Zeng, R.; Chen, G.; DiSalvo, F. J.; Muller, D. A.; Abruña, H. D. Octahedral Spinel Electrocatalysts for Alkaline Fuel Cells. *Proc. Natl. Acad. Sci. U.S.A.* **2019**, *116*, 24425–24432.
- (3) Janani, G.; Surendran, S.; Choi, H.; Han, M.-K.; Sim, U. In Situ Grown CoMn<sub>2</sub>O<sub>4</sub> 3D-Tetragons on Carbon Cloth: Flexible Electrodes for Efficient Rechargeable Zinc-Air Battery Powered Water Splitting Systems. *Small* **2021**, *17*, 2103613.
- (4) Kim, J.; Ko, W.; Yoo, J. M.; Paidi, V. K.; Jang, H. Y.; Shepit, M.; Lee, J.; Chang, H.; Lee, H. S.; Jo, J.; Kim, B. H.; Cho, S.-P.; Lierop, J.; Kim, D.; Lee, K.-S.; Back, S.; Sung, Y.-E.; Hyeon, T. Structural Insights into Multi-Metal Spinel Oxide Nanoparticles for Boosting Oxygen Reduction Electrocatalysis. *Adv. Mater.* 2022, 34, 2107868.
- (5) Liang, Y.; Wang, H.; Zhou, J.; Li, Y.; Wang, J.; Regier, T.; Dai, H. Covalent Hybrid of Spinel Manganese-Cobalt Oxide and Graphene as Advanced Oxygen Reduction Electrocatalysts. *J. Am. Chem. Soc.* **2012**, 134, 3517–3523.
- (6) Stoerzinger, K. A.; Risch, M.; Han, B.; Shao-Horn, Y. Recent Insights into Manganese Oxides in Catalyzing Oxygen Reduction Kinetics. *ACS Catal.* **2015**, *5*, 6021–6031.
- (7) Wei, C.; Feng, Z.; Scherer, G. G.; Barber, J.; Shao-Horn, Y.; Xu, Z. J. Cations in Octahedral Sites: A Descriptor for Oxygen

- Electrocatalysis on Transition-Metal Spinels. Adv. Mater. 2017, 29, 1606800.
- (8) Zhao, Q.; Yan, Z.; Chen, C.; Chen, J. Spinels: Controlled Preparation, Oxygen Reduction/Evolution Reaction Application, and Beyond. *Chem. Rev.* **2017**, *117*, 10121–10211.
- (9) Li, C.; Han, X.; Cheng, F.; Hu, Y.; Chen, C.; Chen, J. Phase and Composition Controllable Synthesis of Cobalt Manganese Spinel Nanoparticles towards Efficient Oxygen Electrocatalysis. *Nat. Commun.* **2015**, *6*, 7345.
- (10) Cheng, F.; Shen, J.; Peng, B.; Pan, Y.; Tao, Z.; Chen, J. Rapid Room-Temperature Synthesis of Nanocrystalline Spinels as Oxygen Reduction and Evolution Electrocatalysts. *Nat. Chem.* **2011**, *3*, 79–84.
- (11) Wang, H.-Y.; Hung, S.-F.; Chen, H.-Y.; Chan, T.-S.; Chen, H. M.; Liu, B. In Operando Identification of Geometrical-Site-Dependent Water Oxidation Activity of Spinel Co<sub>3</sub>O<sub>4</sub>. *J. Am. Chem. Soc.* **2016**, *138*, 36–39.
- (12) Wang, X.-T.; Ouyang, T.; Wang, L.; Zhong, J.-H.; Liu, Z.-Q. Surface Reorganization on Electrochemically-Induced Zn-Ni-Co Spinel Oxides for Enhanced Oxygen Electrocatalysis. *Angew. Chem., Int. Ed.* **2020**, *59*, 6492–6499.
- (13) Zhou, Y.; Xi, S.; Wang, J.; Sun, S.; Wei, C.; Feng, Z.; Du, Y.; Xu, Z. J. Revealing the Dominant Chemistry for Oxygen Reduction Reaction on Small Oxide Nanoparticles. *ACS Catal.* **2018**, *8*, 673–677
- (14) Wang, H.-Y.; Hsu, Y.-Y.; Chen, R.; Chan, T.-S.; Chen, H. M.; Liu, B. Ni<sup>3+</sup>-Induced Formation of Active NiOOH on the Spinel Ni-Co Oxide Surface for Efficient Oxygen Evolution Reaction. *Adv. Energy Mater.* **2015**, *5*, 1500091.
- (15) Wachs, I. E.; Routray, K. Catalysis Science of Bulk Mixed Oxides. ACS Catal. 2012, 2, 1235–1246.
- (16) Zhang, J.; Yang, H.; Fang, J.; Zou, S. Synthesis and Oxygen Reduction Activity of Shape-Controlled Pt<sub>3</sub>Ni Nanopolyhedra. *Nano Lett.* **2010**, *10*, 638–644.
- (17) Choi, S.-I.; Xie, S.; Shao, M.; Odell, J. H.; Lu, N.; Peng, H.-C.; Protsailo, L.; Guerrero, S.; Park, J.; Xia, X.; Wang, J.; Kim, M. J.; Xia, Y. Synthesis and Characterization of 9 nm Pt-Ni Octahedra with a Record High Activity of 3.3 A/mg<sub>Pt</sub> for the Oxygen Reduction Reaction. *Nano Lett.* **2013**, *13*, 3420—3425.
- (18) Zhang, L.; Roling, L. T.; Wang, X.; Vara, M.; Chi, M.; Liu, J.; Choi, S.-I.; Park, J.; Herron, J. A.; Xie, Z.; Mavrikakis, M.; Xia, Y. Platinum-Based Nanocages with Subnanometer-Thick Walls and Well-Defined, Controllable Facets. *Science* **2015**, 349, 412–416.
- (19) Wang, Y.; Yang, Y.; Jia, S.; Wang, X.; Lyu, K.; Peng, Y.; Zheng, H.; Wei, X.; Ren, H.; Xiao, L.; Wang, J.; Muller, D. A.; Abruña, H. D.; Hwang, B. J.; Lu, J.; Zhuang, L. Synergistic Mn-Co Catalyst Outperforms Pt on High-Rate Oxygen Reduction for Alkaline Polymer Electrolyte Fuel Cells. *Nat. Commun.* **2019**, *10*, 1506.
- (20) Wang, X.-T.; Ouyang, T.; Wang, L.; Zhong, J.-H.; Ma, T.; Liu, Z.-Q. Redox-Inert Fe<sup>3+</sup> Ions in Octahedral Sites of Co-Fe Spinel Oxides with Enhanced Oxygen Catalytic Activity for Rechargeable Zinc-Air Batteries. *Angew. Chem., Int. Ed.* **2019**, *58*, 13291–13296.
- (21) Zhou, Y.; Du, Y.; Xi, S.; Xu, Z. J. Spinel Manganese Ferrites for Oxygen Electrocatalysis: Effect of Mn Valency and Occupation Site. *Electrocatalysis* **2018**, *9*, 287–292.
- (22) Zhu, C.; Fu, S.; Du, D.; Lin, Y. Facilely Tuning Porous NiCo<sub>2</sub>O<sub>4</sub> Nanosheets with Metal Valence-State Alteration and Abundant Oxygen Vacancies as Robust Electrocatalysts Towards Water Splitting. *Chem. Eur. J.* **2016**, 22, 4000–4007.
- (23) Paudel, T. R.; Zakutayev, A.; Lany, S.; d'Avezac, M.; Zunger, A. Doping Rules and Doping Prototypes in A<sub>2</sub>BO<sub>4</sub> Spinel Oxides. *Adv. Funct. Mater.* **2011**, *21*, 4493–4501.
- (24) Zhou, Y.; Sun, S.; Wei, C.; Sun, Y.; Xi, P.; Feng, Z.; Xu, Z. J. Significance of Engineering the Octahedral Units to Promote the Oxygen Evolution Reaction of Spinel Oxides. *Adv. Mater.* **2019**, *31*, 1902509.
- (25) Peng, S.; Gong, F.; Li, L.; Yu, D.; Ji, D.; Zhang, T.; Hu, Z.; Zhang, Z.; Chou, S.; Du, Y.; Ramakrishna, S. Necklace-like Multishelled Hollow Spinel Oxides with Oxygen Vacancies for

- Efficient Water Electrolysis. J. Am. Chem. Soc. 2018, 140, 13644-13653.
- (26) Li, Y.; Shen, W. Morphology-Dependent Nanocatalysts: Rod-Shaped Oxides. *Chem. Soc. Rev.* **2014**, *43*, 1543–1574.
- (27) Cudennec, Y.; Lecerf, A. The Transformation of Cu(OH)<sub>2</sub> into CuO, Revisited. *Solid State Sci.* **2003**, *5*, 1471–1474.
- (28) Zhu, J.; Bi, H.; Wang, Y.; Wang, X.; Yang, X.; Lu, L. CuO Nanocrystals with Controllable Shapes Grown from Solution without Any Surfactants. *Mater. Chem. Phys.* **2008**, *109*, 34–38.
- (29) Zhang, Q.; Zhang, K.; Xu, D.; Yang, G.; Huang, H.; Nie, F.; Liu, C.; Yang, S. CuO Nanostructures: Synthesis, Characterization, Growth Mechanisms, Fundamental Properties, and Applications. *Prog. Mater. Sci.* **2014**, *60*, 208–337.
- (30) Tian, Z.-R.; Tong, W.; Wang, J.-Y.; Duan, N.-G.; Krishnan, V. V.; Suib, S. L. Manganese Oxide Mesoporous Structures: Mixed-Valent Semiconducting Catalysts. *Science* **1997**, *276*, 926–930.
- (31) Choi, S.-I.; Lee, S. R.; Ma, C.; Oliy, B.; Luo, M.; Chi, M.; Xia, Y. Facile Synthesis of Rhodium Icosahedra with Controlled Sizes up to 12 nm. *ChemNanoMat* **2016**, *2*, 61–66.
- (32) Li, P.; Nan, C.; Wei, Z.; Lu, J.; Peng, Q.; Li, Y. Mn3O4 Nanocrystals: Facile Synthesis, Controlled Assembly, and Application. *Chem. Mater.* **2010**, 22, 4232–4236.
- (33) Godillot, G.; Guerlou-Demourgues, L.; Croguennec, L.; Shaju, K. M.; Delmas, C. Effect of Temperature on Structure and Electronic Properties of Nanometric Spinel-Type Cobalt Oxides. *J. Phys. Chem.* C 2013, 117, 9065–9075.
- (34) Ndione, P. F.; Shi, Y.; Stevanovic, V.; Lany, S.; Zakutayev, A.; Parilla, P. A.; Perkins, J. D.; Berry, J. J.; Ginley, D. S.; Toney, M. F. Control of the Electrical Properties in Spinel Oxides by Manipulating the Cation Disorder. *Adv. Funct. Mater.* **2014**, 24, 610–618.
- (35) Zhou, Y.; Sun, S.; Xi, S.; Duan, Y.; Sritharan, T.; Du, Y.; Xu, Z. J. Superexchange Effects on Oxygen Reduction Activity of Edge-Sharing  $[Co_xMn_{1-x}O_6]$  Octahedra in Spinel Oxide. *Adv. Mater.* **2018**, 30, 1705407.
- (36) Shoemaker, D. P.; Li, J.; Seshadri, R. Unraveling Atomic Positions in an Oxide Spinel with Two Jahn—Teller Ions: Local Structure Investigation of CuMn<sub>2</sub>O<sub>4</sub>. *J. Am. Chem. Soc.* **2009**, *131*, 11450—11457.
- (37) Sinha, A. P. B.; Sanjana, N. R.; Biswas, A. B. The Crystal Structure of Copper Manganite. *J. Phys. Chem.* **1958**, *62*, 191–194.
- (38) Miller, A. Determination of the Valence State of Copper in Cubic CuMn<sub>2</sub>O<sub>4</sub> spinel by X-ray Absorption Edge Measurements. *J. Phys. Chem. Solids* **1968**, *29*, 633–639.
- (39) Wang, X.; Pan, Z.; Chu, X.; Huang, K.; Cong, Y.; Cao, R.; Sarangi, R.; Li, L.; Li, G.; Feng, S. Atomic-Scale Insights into Surface Lattice Oxygen Activation at the Spinel/Perovskite Interface of Co<sub>3</sub>O<sub>4</sub>/La<sub>0.3</sub>Sr<sub>0.7</sub>CoO<sub>3</sub>. *Angew. Chem., Int. Ed.* **2019**, *58*, 11720–11725.
- (40) Agyeman, D. A.; Zheng, Y.; Lee, T.-H.; Park, M.; Tamakloe, W.; Lee, G.-H.; Jang, H. W.; Cho, K.; Kang, Y.-M. Synergistic Catalysis of the Lattice Oxygen and Transition Metal Facilitating ORR and OER in Perovskite Catalysts for Li-O<sub>2</sub> Batteries. *ACS Catal.* **2021**, *11*, 424–434.
- (41) Zhao, S.; Yu, H.; Maric, R.; Danilovic, N.; Capuano, C. B.; Ayers, K. E.; Mustain, W. E. Calculating the Electrochemically Active Surface Area of Iridium Oxide in Operating Proton Exchange Membrane Electrolyzers. *J. Electrochem. Soc.* **2015**, *162*, F1292–F1298.
- (42) Connor, P.; Schuch, J.; Kaiser, B.; Jaegermann, W. The Determination of Electrochemical Active Surface Area and Specific Capacity Revisited for the System MnOx as an Oxygen Evolution Catalyst. Z. Phys. Chem. 2020, 234, 979—994.
- (43) Cossar, E.; Houache, M. S. E.; Zhang, Z.; Baranova, E. A. Comparison of Electrochemical Active Surface Area Methods for Various Nickel Nanostructures. *J. Electroanal. Chem.* **2020**, 870, 114246.
- (44) Yang, Y.; Wang, Y.; Xiong, Y.; Huang, X.; Shen, L.; Huang, R.; Wang, H.; Pastore, J. P.; Yu, S.-H.; Xiao, L.; Brock, J. D.; Zhuang, L.; Abruña, H. D. In Situ X-ray Absorption Spectroscopy of a Synergistic

- Co-Mn Oxide Catalyst for the Oxygen Reduction Reaction. J. Am. Chem. Soc. 2019, 141, 1463–1466.
- (45) Xiong, Y.; Yang, Y.; Feng, X.; DiSalvo, F. J.; Abruña, H. D. A Strategy for Increasing the Efficiency of the Oxygen Reduction Reaction in Mn-Doped Cobalt Ferrites. *J. Am. Chem. Soc.* **2019**, *141*, 4412–4421.
- (46) Yang, Y.; Zeng, R.; Xiong, Y.; DiSalvo, F. J.; Abruña, H. D. Cobalt-Based Nitride-Core Oxide-Shell Oxygen Reduction Electrocatalysts. *J. Am. Chem. Soc.* **2019**, *141*, 19241–19245.
- (47) Yousefi, E.; Ghorbani, M.; Dolati, A.; Yashiro, H.; Outokesh, M. Preparation of New Titanium Nitride-Carbon Nanocomposites in Supercritical Benzene and Their Oxygen Reduction Activity in Alkaline Medium. *Electrochim. Acta* 2015, 164, 114–124.

## Recommended by ACS

Ru-Substituted MnO<sub>2</sub> for Accelerated Water Oxidation: The Feedback of Strain-Induced and Polymorph-Dependent Structural Changes to the Catalytic Activity and Mechanism

Yongze Qin, Zhao Deng, et al.

DECEMBER 15, 2022

ACS CATALYSIS

READ 🗷

Efficient Electrocatalytic Oxidation of Glycerol via Promoted OH\* Generation over Single-Atom-Bismuth-Doped Spinel  $\text{Co}_3\text{O}_4$ 

Ye Wang, Haohong Duan, et al.

SEPTEMBER 28, 2022

ACS CATALYSIS

READ 🗹

Unveiling a Surface Electronic Descriptor for Fe-Co Mixing Enhanced the Stability and Efficiency of Perovskite Oxygen Evolution Electrocatalysts

Yongchul Kim, Geunsik Lee, et al.

NOVEMBER 16, 2022

ACS CATALYSIS

READ 🗹

Ceria-Promoted Reconstruction of Ni-Based Electrocatalysts toward Efficient Oxygen Evolution

Zinan Huang, Qingsheng Gao, et al.

OCTOBER 28, 2022

ACS CATALYSIS

READ 🗹

Get More Suggestions >